



Physical and Aerodynamic Characterization of Particle Clusters at Sakurajima Volcano (Japan)

Pietro Gabellini^{1*}, Eduardo Rossi², Costanza Bonadonna², Marco Pistolesi³, Gholamhossein Bagheri^{2,3,4} and Raffaello Cioni¹

¹ Dipartimento di Scienze della Terra, Università di Firenze, Florence, Italy, ² Département des Sciences de la Terre, Université de Genève, Geneva, Switzerland, ³ Dipartimento di Scienze della Terra, Università di Pisa, Pisa, Italy, ⁴ Abteilung für Hydrodynamik, Max Planck Institute, Göttingen, Germany

The process of particle aggregation significantly affects ash settling dynamics associated with volcanic explosive eruptions. Several experiments have been carried out to investigate the physics of ash aggregation and dedicated numerical schemes have been developed to produce more accurate forecasting of ash dispersal and sedimentation. However, numerical description of particle aggregation is complicated by the lack of complete datasets on natural samples required for model validation and calibration. Here we present a first comprehensive dataset for the internal structure, aerodynamical properties (e.g., size, density, terminal velocity) and grain size of constituting particles of a variety of aggregate types collected in the natural laboratory of Sakurajima Volcano (Japan). Even though the described particle clusters represent the most common types of aggregates associated with ash-rich fallouts, they are of difficult characterization due to the very low potential of preservation in tephra-fallout deposits. Properties were, therefore, derived based on a combination of high-resolution-high-speed videos of tephra fallout, scanning electron microscope analysis of aggregates collected on adhesive paper and analysis of tephra samples collected in dedicated trays. Three main types of particle clusters were recognized and quantitatively characterized: cored clusters (PC3), coated particles (PC2), and ash clusters (PC1) (in order of abundance). A wide range of terminal velocities (0.5–4 m/s) has been observed for these aggregates, with most values varying between 1 and 2 m/s, while aggregate size varies between 200 and 1,200 μm . PC1, PC2, and PC3 have densities between 250 and 500, 1,500 and 2,000, and 500 and 1,500 kg/m^3 , respectively. The size of the aggregate core, where present, varies between 200 and 750 μm and increases with aggregate size. Grain size of tephra samples was deconvoluted into a fine and a coarse Gaussian subpopulation, well correlated with the grain size of shells and of the internal cores of aggregates, respectively. This aspect, together with the revealed abundance of PC3 aggregates, reconciles the presence of a large amount of fine ash (aggregate shells) with coarse ash (aggregate cores) and better explains the grain size distribution bimodality, the high settling velocity with respect to typical PC1 velocities and the low settling velocities of large aggregates with respect to typical PC2 velocity. Furthermore, ash forming the aggregates was shown to be always finer than 45 μm , confirming the key role played by aggregation processes in fine ash deposition at Sakurajima.

Keywords: ash aggregation, volcanic aggregates, aggregate grain size, tephra dispersal, tephra sedimentation, high-speed camera, image analysis

OPEN ACCESS

Edited by:

Roberto Sulpizio,
University of Bari Aldo Moro, Italy

Reviewed by:

Alison Claire Rust,
University of Bristol, United Kingdom
Daniela Mele,
University of Bari Aldo Moro, Italy

*Correspondence:

Pietro Gabellini
pietro.gabellini@unifi.it

Specialty section:

This article was submitted to
Volcanology,
a section of the journal
Frontiers in Earth Science

Received: 24 June 2020

Accepted: 02 September 2020

Published: 05 October 2020

Citation:

Gabellini P, Rossi E, Bonadonna C, Pistolesi M, Bagheri G and Cioni R (2020) Physical and Aerodynamic Characterization of Particle Clusters at Sakurajima Volcano (Japan). *Front. Earth Sci.* 8:575874. doi: 10.3389/feart.2020.575874

INTRODUCTION

In the last 30 years, several studies reported accurate descriptions of ash aggregates observed during fallout or in pyroclastic deposits of past eruptions (Brown et al., 2012 and references therein). The importance of aggregation on ash dispersal is widely recognized by the scientific community also considering the significant hazards posed to aviation, agriculture and public health by ash fallout (Guffanti et al., 2010; Bonadonna et al., 2012; Jenkins et al., 2015). As a result, many efforts have been made to improve the description of aggregates and our understanding of aggregation processes (e.g., Gilbert and Lane, 1994; James et al., 2002; James et al., 2003; Durant et al., 2009; Bonadonna et al., 2011; Rose & Durant, 2011; Taddeucci et al., 2011; Brown et al., 2012; Van Eaton et al., 2012; Van Eaton and Wilson, 2013; Bagheri et al., 2016; Burns et al., 2017; Vogel et al., 2019), as well as to provide increasingly accurate numerical descriptions for more effective hazard assessments (Cornell et al., 1983; Veitch and Woods, 2001; Bonadonna et al., 2002a; Textor et al., 2006; Costa et al., 2010). Despite the importance of aggregation, due to the low preservation potential of particle clusters in tephra-fallout deposits, only a few examples exist that document the fundamental physical and aerodynamic parameters of ash aggregates, such as their bulk density, terminal velocity and size distribution of the constitutive particles (Bonadonna et al., 2002b; Bonadonna et al., 2011; Taddeucci et al., 2011; Van Eaton et al., 2012; Bagheri et al., 2016; Burns et al., 2017; Miwa et al., 2020). The lack of detailed and ground-based data for ash aggregates importantly affects the reliability of numerical model results (Brown et al., 2012; Durant et al., 2015).

Recently, the direct filming of aggregates during tephra fallout has emphasized the importance of a field-based approach to study particle clusters. In fact, such a strategy allows for physical and aerodynamic parameters of particle clusters to be derived before their disruption at the moment of impact with the ground (Taddeucci et al., 2011; Bagheri et al., 2016; Miwa et al., 2020). For this reason, in this study, we have adopted the state-of-the-art technique involving a high-speed, high-resolution (HS-HR) camera coupled with ground observations and ash collection on adhesive paper aimed at the detailed characterization of aggregates (Bagheri et al., 2016). This approach proved to be fundamental for an accurate description of the internal structure and aerodynamics of aggregates. In fact, field-based strategies based on the collection of aggregates during fallout (e.g., Sorem, 1982; Bonadonna et al., 2002b; Bonadonna et al., 2011; Bagheri et al., 2016) already provided important insights that could not be derived from deposit observations only (e.g., characterization of particle clusters that typically break at the moment of impact with the ground). Nonetheless, specific aerodynamic features (terminal velocity, morphology of falling aggregates) and identification of aggregate types can only be described based on HS-HR videos.

In this work we provide a large dataset of 62 HS-HR video-footages of falling objects (i.e., single particles and particle clusters) collected during a sequence of Vulcanian explosions at Sakurajima volcano (Japan). The combination of the HS-HR videos of falling aggregates with their analysis provided through

the SEM has the main advantage to provide an unbiased description of the aggregates and their constituents before and after their impact on the adhesive paper. Video analysis of falling aggregates prior to their impact is important to measure their terminal velocity and size, which in turn give constraints on bulk density. On the other hand, the collection of aggregates on adhesive paper is needed for further analyses with the SEM, to provide a description of the population of particles forming each aggregate through specific image analysis techniques. The latter allowed the estimation of the grain size distribution (GSD) of either the complete aggregate or only of the external layer of coated ash particles. As a matter of fact, while most of the shell is preserved on the adhesive paper, one or more (up to 4) large particles generally bounce away upon impact. Their main properties can only be derived from the analysis of the HS-HR camera footages. The analysis of the video footages returned an unprecedented and statistically solid database of the physical parameters governing the sedimentation dynamics of aggregates and allowed better constraints on their internal structure and characteristics with respect to previous studies (e.g., Bonadonna et al., 2011; Taddeucci et al., 2011; Brown et al., 2012; Bagheri et al., 2016; Miwa et al., 2020). The presented results, although specific for Sakurajima volcano, provide a first comprehensive database of physical parameters of particle clusters never collected before with such a detail. The statistical treatment and the large number of investigated clusters make such a dataset a reference for aggregation studies associated with mid-intensity, ash-dominated eruptions as well as for the validation and calibration of numerical schemes that describe particle aggregation.

Sakurajima Volcano

Sakurajima Volcano (Japan) is one of the most active volcanoes of the world, with a persistent activity that started in 1955 and is continuing to present days. The typical activity consists of repeated Vulcanian explosions of various intensity occurring with an almost daily frequency from both Minamidake summit crater and, since June 2006, Showa crater, on the eastern flank of the volcano. Explosions are generally associated with the production of large amounts of ash (Oba et al., 1980; Ishihara 1985; Iguchi et al., 2008; Yamanoi et al., 2008; Miwa et al., 2013a). After a brief interruption between August 2015 and February 2016, activity renewed firstly at Showa crater with small explosive events, before shifting again to Minamidake crater during March 2016, with higher intensity explosions (<http://www.data.jma.go.jp/obd/stats/etrn/index.php>). Since 2016, activity alternated between the two vents, with variable energy, intensity, and frequency. The highly populated urban area of Kagoshima city lies ~10 km from the volcano, which represents a primary source of hazard for both the local population and civil aviation due to its continuous emission of large amounts of ash. On the other hand, for the high frequency of the activity characterized by the nearly daily injection in the atmosphere of a large amount of ash, Sakurajima represents a unique, natural laboratory for the investigation of volcanic ash dispersal, aggregation and fallout and for the study of the implications on life and safety in highly urbanized contexts.

METHODS

Different types of samples were collected at Sakurajima volcano during several Vulcanian explosions occurred between the July 28 and the August 3, 2013 (Table 1). In detail, the examined dataset consists of: 1) HS-HR video footages of falling ash aggregates; 2) aggregates collected on adhesive papers; and 3) tephra samples accumulated in dedicated trays.

All the sampling sites are located downwind of the active vent (i.e., Showa crater), approximately along the dispersal axis at a distance of about 5 km from the crater (Figure 1; Supplementary Table S1). Timing of most videos (53 out of 62) is synchronous with tephra sampling (Supplementary Table S3). As reported by the Japan Meteorological Agency (JMA), the activity of Sakurajima in that period was defined as “high level,” with around 10 major explosions recorded per week from the Showa crater. During the 5-day-long sampling period, the height of the eruption plumes ranged between 1.5 and 3 km above sea level. The observed activity was a series of Vulcanian explosions, associated with low-to-moderate ash emissions and ash venting (Yamanoi et al., 2008; Miwa et al., 2009). The wind direction and intensity at different heights above sea level (<http://weather.uwyo.edu/upperair/sounding.html>) is presented in Figure 2, together with indication of meteorological conditions during the same period. Wind conditions (Figure 2A) remained almost constant both in direction (eastward) and intensity throughout the entire study period, while atmospheric parameters (Figure 2B) showed significant daily variations. Despite this, the collection of aggregates and of HS-HR videos was carried out under very similar meteorological conditions.

Field Setup and Analysis of the High-Speed, High-Resolution Videos

The aggregates were filmed while falling using a Phantom Pro HS-Camera equipped with a Nikon 60 mm f/2.8 D AF Micro Nikkor lens. These were sampled on a 2 × 2.5 cm sheet of adhesive paper placed within the camera field of view. A detailed description of the field setup can be found in Figure 3 of Bagheri et al. (2016). A total of 62 HS-HR videos were selected and analyzed with Fiji software (Schindelin et al., 2012); see Supplementary Section S2 for further descriptions on the video selection and analysis, and S5 for selected HS-HR videos of falling aggregates. Aggregate size, terminal velocity and density were estimated following different methodological approaches (Table 1); associated errors and uncertainties to the derived quantities are addressed in Supplementary Section S3.

Size and Shape of Aggregates and Cores

Size and shape of aggregates were characterized based on HS-HR videos by considering only the best-focused frames. Since the aggregates observed in the video were not exactly spherical, we adopted the method proposed by Bagheri and Bonadonna (2016) for the estimation of aggregate dimension (*D*). Equation 1 was used considering three shape parameters (*L*, *I*, and *S*):

TABLE 1 | Overview of the different measurements (first column from the left) together with the related methodology used for the sample acquisition and for the derivation of related quantities.

Data	Origin of the data	Size	Shape	Density	Terminal velocity
Aggregates observed with HS-HR setup	Image analysis on the HS-HR video	Measured as the diameter of the equivalent circle from HS-HR videos (averaging the area along all the frames)	<i>L</i> , <i>I</i> , and <i>S</i> measured directly from HS-HR video	Derived from the formal equation of <i>V_t</i>	Measured comparing the changing position of particles along <i>Y</i> axis in different frames of HS-HR video
Internal cores of aggregates	Image analysis on the post-rebound frames in the video + manual collection	Measured from post-rebound frames in the video with ImageJ as the diameter of the equivalent circle	<i>L</i> , <i>I</i> and <i>S</i> measured from post-rebound frames in the video with ImageJ	Directly measured with a water pycnometer	Calculated using the formal equation of <i>V_t</i>
Fine ash coating (external shell)	SEM investigation of the adhesive paper located in front of the HS-HR setup	Size represents the mean mode of the GSD derived from image analysis of SEM images (<i>L</i> = <i>I</i> = <i>S</i> = 0)	Considered as spherical (<i>L</i> = <i>I</i> = <i>S</i> = 0)	Assumed equal to the density of the cores (i.e., measured with water pycnometer) and corrected for difference in size	Same as above
Tephra sample in trays: Coarse mode	CILAS analysis + deconvolution of the obtained GSDs as a sum of Gaussian subpopulations (SPs)	Size represents the mean value of the coarse mode characterizing the deposit	Considered as spherical (<i>L</i> = <i>I</i> = <i>S</i> = 0)	Same as above	Same as above
Tephra sample in trays	CILAS analysis + deconvolution of the GSDs using MagicPlot	Size represents the mean value of the fine mode characterizing the deposit	Considered as spherical (<i>L</i> = <i>I</i> = <i>S</i> = 0)	Same as above	Same as above

GSD, grain size distribution; HS-HR, high-speed, high-resolution; *V_t*, terminal Velocity (Eq. 2)

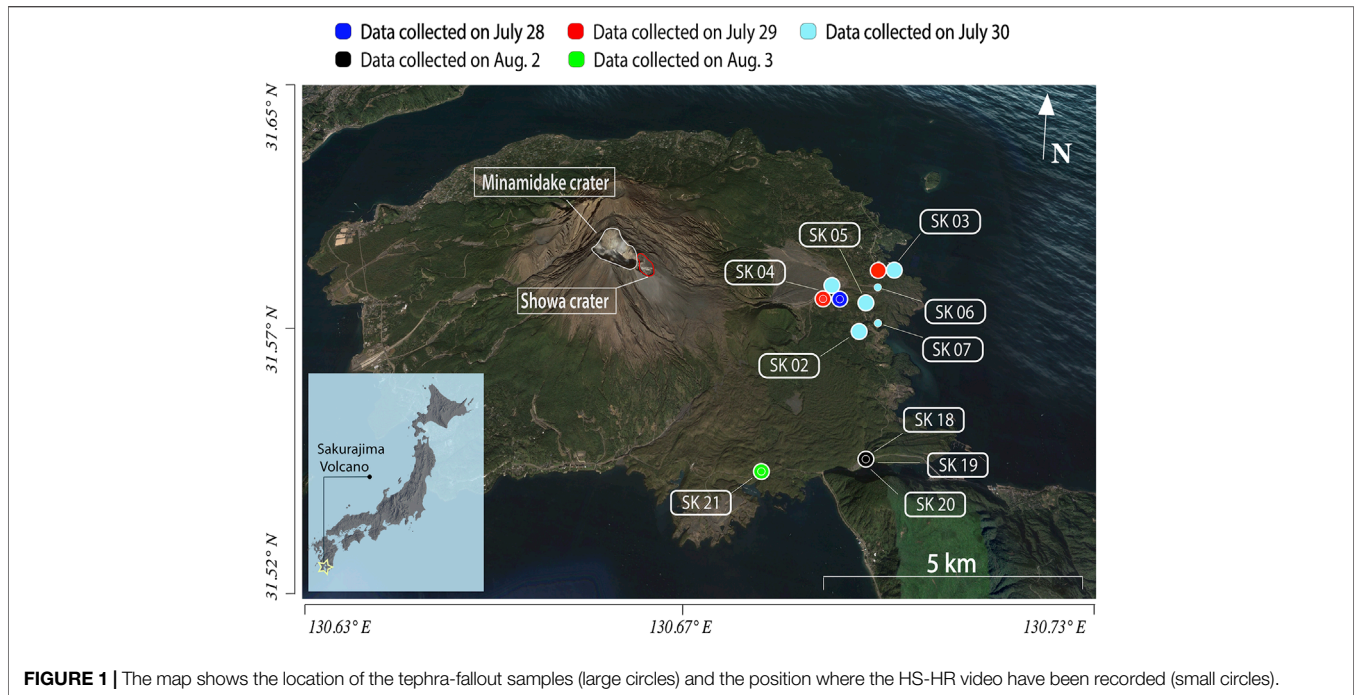


FIGURE 1 | The map shows the location of the tephra-fallout samples (large circles) and the position where the HS-HR video have been recorded (small circles).

$$d_{eq} = 0.928 \cdot (L \cdot I \cdot S)^{1/3} \quad (1)$$

The three dimensionless parameters (L , I , and S) were chosen to account for the complex morphology of the aggregates (Bagheri and Bonadonna, 2016); if adequately combined they define the Flatness and Elongation of the particle (Flatness: S/I ; Elongation: I/L). L , I , and S enter in the definition of the drag coefficient (C_d) which was calculated according to Eq. 34 of Bagheri and Bonadonna (2016). They were defined considering only the aggregate projections with maximum and minimum areas, according to new the approach introduced by Bagheri and Bonadonna (2016). In particular, L and I are defined respectively as the maximum and minimum Feret diameters (calipers) measured on the maximum-area projection, while S corresponds to the minimum Feret diameter measured on the minimum-projection area. Since aggregates were typically observed while rotating, and thus offering different face-projections to the camera, the parameters were calculated considering the different aggregates projections inferred from videos during the settling. Aggregate dimension was also estimated by assuming the shape as spherical: the equivalent diameter was calculated by averaging the area in pixel of the different aggregate projections revealed within the frames of the videos. For spherical aggregates either one of the calculated diameters can be used without differences, but for natural (i.e., irregular) aggregates using the diameter estimated with the spherical assumption can lead to considerable errors in the determination of aggregate density.

As already reported by Bagheri et al. (2016), a large number of aggregates were observed to disaggregate after colliding with the adhesive paper. In most of the cases, the observed aggregates show the presence of coarse cores that usually bounce away after

the impact, leaving the particles forming the external shell attached to the adhesive paper. In 15 cases out of the 62 analyzed videos, we were able to measure both the grain size of the shell of the aggregate left on the adhesive paper and the size and shape of the rebounding core. The difference between the diameter of the aggregate (inferred prior the landing on the adhesive paper) and that of the associated cores (inferred from post-rebound frames of the videos) was calculated to derive the average thickness and the volume fraction of the shell.

Estimate of Aggregate and Core Density

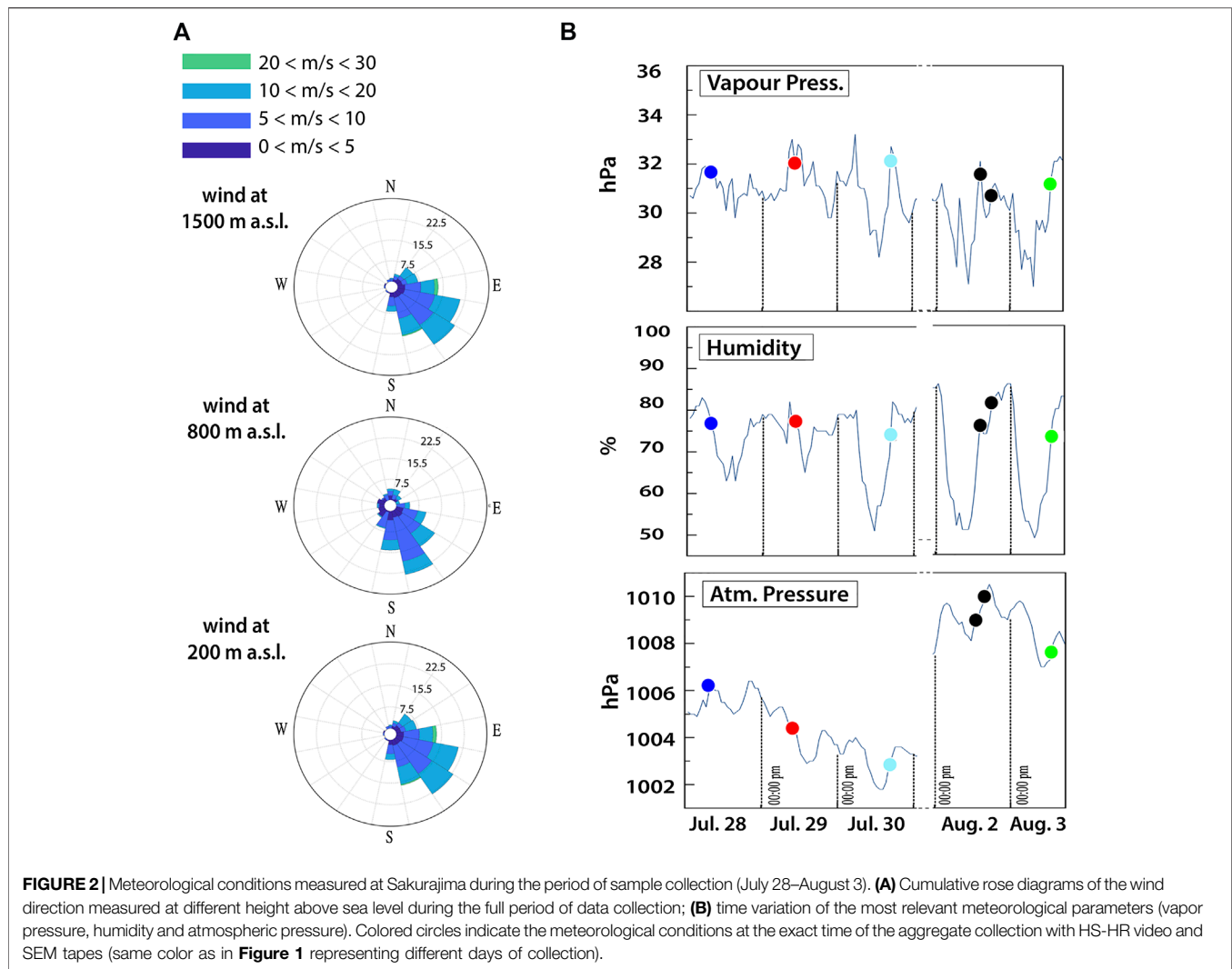
The measure of the terminal velocity and size of a given object allows the bulk density of the aggregate to be constrained from:

$$\rho_p = \frac{3}{4} \frac{C_d \rho_a V_t^2}{g d_{eq}} + \rho_a \quad (2)$$

where d_{eq} is the particle equivalent diameter, ρ_p is the density of the falling particles, ρ_a is the surrounding fluid density, V_t is the particle terminal velocity, and C_d is the drag coefficient, defined considering the three shape parameters L , I , and S . The air density is taken constant and equal to $\rho_a = 1.177 \text{ kg/m}^3$; the kinematic viscosity of the air is $\nu_a = 1.568 \times 10^{-5} \text{ m}^2/\text{s}$ (<http://weather.uwyo.edu/upperair/sounding.html>).

Since aggregate density is a derived quantity having a non-linear relation with the measured terminal velocity, shape, size, and air density, we used a Monte Carlo simulation in order to provide a better estimation of the density, also considering the uncertainties related to the different variables entering in Eq. 2 (see **Supplementary Section S3.1**).

Density of the core was calculated using the size-vs.-density trend reported in **Figure 4** of Bagheri and Bonadonna (2016).



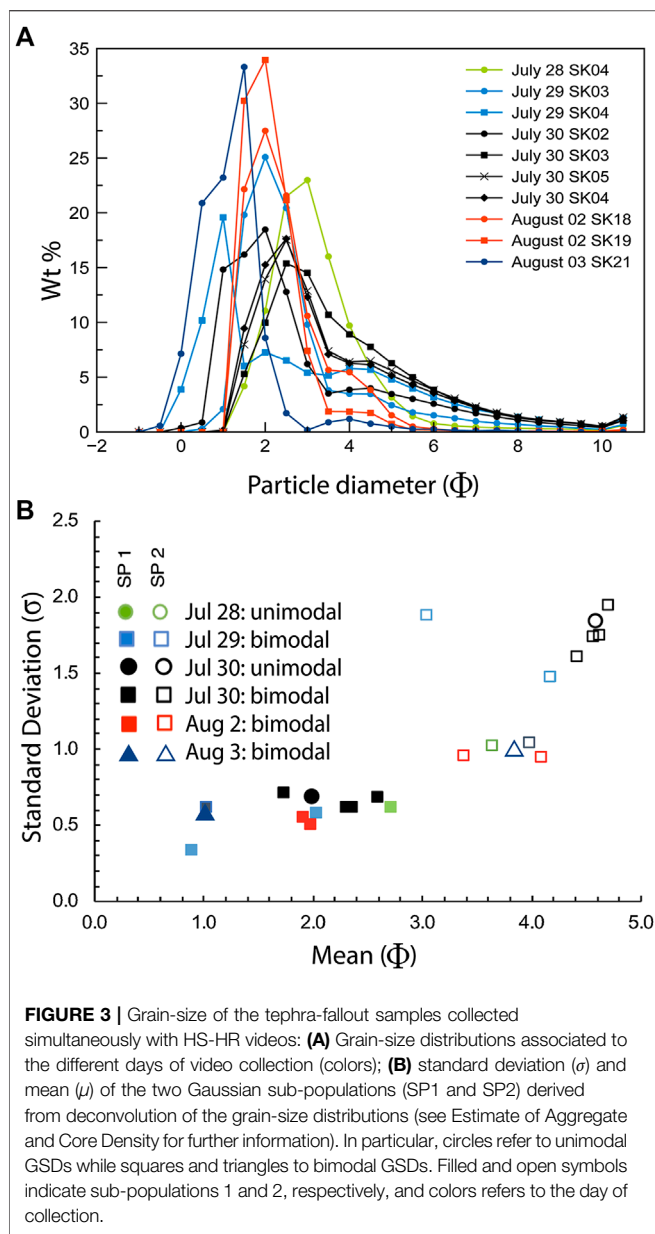
Grain Size Analysis of Aggregates Collected on Adhesive Paper

A subset of the aggregates filmed and collected on adhesive paper was analyzed with the SEM, extracting information on the aggregate type, the GSD of the shell and, where still preserved, the dimension of the core that was measured through video analysis. The GSD of the shell, combined with the information about the size of the inner core, where present, provides a reliable picture of the total GSD of each aggregate prior to the impact. The technique used for the determination of the GSD consists of: 1) manual contouring of the ash particles from SEM images using Fiji; 2) estimation of the area of each particle and of the related equivalent circle diameter; and 3) conversion of diameters number frequency for classes of size into volume frequency data. The volume-based GSD of each aggregate shell was then described as a sum of two independent Gaussian subpopulations: a coarse-grained subpopulation (SP1) and a fine grained one (SP2). The fitting operations are obtained by means of a residual minimization algorithm using the MagicPlot software ([https://](https://magicplot.com)

magicplot.com). The modal value, the graphical skewness and the ratio between the fraction of the coarse (SP2) and the fine (SP1) subpopulations, hereafter defined as SP-ratio, were used to characterize the GSD of each aggregate shell.

Grain Size Analysis of Tephra Samples

A set of tephra samples was collected in the days between July 28 and August 3, 2013 placing 40 × 28 cm plastic trays at various locations (**Figure 1**; **Supplementary Table S1**). The tephra samples analyzed for GSD (**Figure 3**) were collected, at the same time and location of the samples collected on adhesive paper, successively analyzed with SEM, and videos acquired with HS-HR camera (**Figure 1**). Multiple tephra samples were collected on July 30 during the same event at different locations (SK02-03-04-05; cyan empty circles in **Figure 1**) with respect to the synchronous HS-HR videos (SK06-07; cyan filled dots in **Figure 1**). The closest collection point of tephra samples is located in this case about 200 m from the HS-HR camera setup. The GSD of the different samples was derived



combining mechanical sieving (for particles larger than 500 μm in diameter) and laser-diffraction analysis using a CILAS 1180 particle-size analyser (for particles $<500 \mu\text{m}$). As in the case of the aggregate shells, the GSDs of tephra samples were all deconvoluted into the sum of two Gaussian subpopulations SP1 and SP2, always getting $R^2 > 0.94$ (Table 2). Each subpopulation was then described in terms of mean (μ), standard deviation (σ) and mass fraction (in percent with respect to the total sample).

RESULTS

Grain Size Distribution of Tephra Samples

The adopted sampling strategy resulted in a close spatial and temporal correspondence between the information derived from

tephra samples collected in trays (reported in Figure 3 and summarized in Table 2), the information derived from SEM analyses on aggregates collected on adhesive tapes (Figure 4; Table 3) and the information of the falling aggregates extracted from the analysis of the HS-HR videos (Figure 5; Supplementary Table S3).

Most of the analyzed tephra samples show similar, clearly bimodal GSD with a main mode peaked around $1-2.5\phi$, and a secondary mode ranging between 4 and 4.5ϕ (Figure 3A). Only two samples (July 28 SK04 and July 30 SK03) show a unimodal, positively skewed distribution with the mode peaked at about 2.5 and 3ϕ , respectively. In addition, the sample SK04 of July 29 is characterized by three modes: a primary mode at 1ϕ , and two poorly prominent secondary modes at 2 and 4.5ϕ , respectively. Regardless of the GSD type (i.e., unimodal or polymodal), all the distributions were deconvoluted, with low residuals (Table 2), into a coarse (SP1) and a fine (SP2) subpopulation, described in terms of mean, standard deviation and weight fraction (Figure 3B; Table 2). It is interesting to note that the relative weight of each SP, for samples collected during the same event, is dependent on sampling position with respect to the dispersal axis (Table 2): the relative amount of the finer-grained SP2 shows a sharp cross-wind increase (e.g., tephra samples collected at SK02 and SK03 on July 30, or at SK03 and SK04 on July 29; Table 2). Moreover, the relative weight of each SP depends also on the day of collection, and hence probably on the eruptive conditions (e.g., wt% of SP1 of the August 3 tephra sample is significantly larger with respect to all the others; Table 2).

Types of Aggregates from Visual Observations

Three different types of aggregates were identified during the period of data collection. Visual observations were accomplished thanks to the analysis of the HS-HR camera videos coupled with the investigation, using stereo microscope and SEM analysis, of the collected adhesive papers. The occurrence of the identified aggregate types was also confirmed by the critical interpretation of aerodynamic data, obtained from the analysis of the HS-HR videos (Figure 5; Supplementary Table S3):

- PC1 [Ash Clusters of Brown et al. (2012)]: ash aggregates of irregular shape and variable size (from around 400 up to 1,200 μm), formed by fine ash. This type of aggregate represents 10–15% of aggregates analyzed through videos (Figure 5); unfortunately, the presence and abundance of PC1 aggregates was inferred only from HS-HR video since no PC1 was directly collected on adhesive paper.
- PC2 [Coated Particles of Brown et al. (2012)]: large particles ($>200 \mu\text{m}$) partially covered by fine ash (on average $<20 \mu\text{m}$) forming a thin shell coating the external surface. Aerodynamical behavior of discontinuously covered single particles can be considered an end-member of this category (about 25–30% of all aggregates observed in videos, Figure 5).
- PC3 [Cored Clusters of Bagheri et al. (2016)]: aggregates ($>200 \mu\text{m}$) characterized by a significant amount of

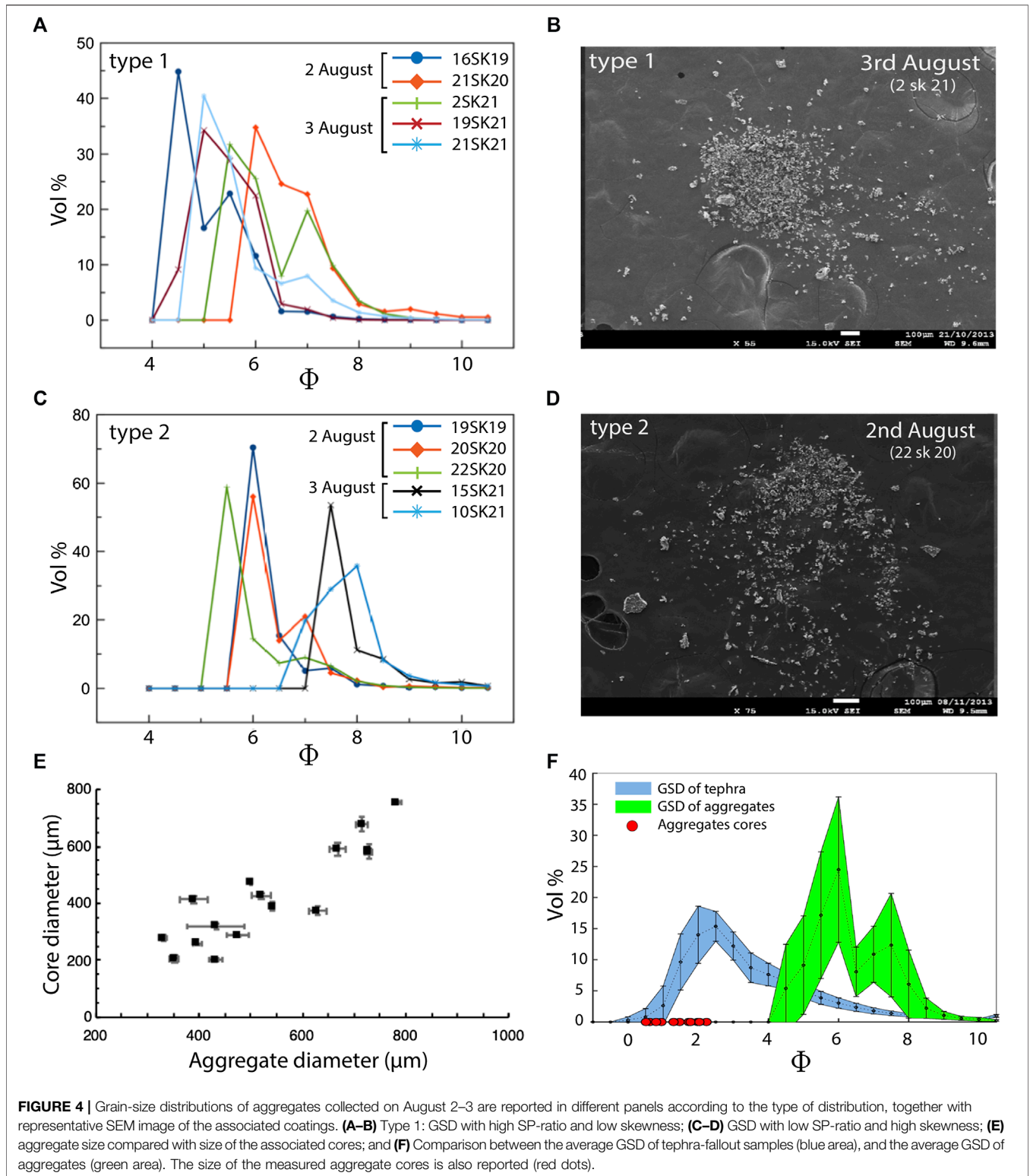


TABLE 2 | Information relative to tephra samples collected in dedicated trays.

Day of collection	Eruption time (JST)	Collect. time (JST)	Distance from the dispersal axis (km)	Sample location	GSD mode (ϕ)	Mean (SP1) (ϕ)	Fraction (SP1) (wt%)	Mean (SP2) (ϕ)	Fraction (SP2) (wt%)	R ²
July 28	Nd	11.50–12.04	~0.3	SK04	3.0	2.7	58	3.6	42	0.978
July 29	11.10	11.19–11.31	~0.2	SK03	2.0	2.0	75	4.2	25	0.979
		11.19–11.31	~0.9	SK04	1.0	1.1	25	4.0	75	0.988
July 30	17.03	14.43–19.24	~1.4	SK03	2.5	2.6	42	4.4	58	0.982
		15.30–19.03	~0.3	SK02	2.0	1.7	62	4.4	38	0.950
		16.25–19.19	~0.6	SK05	2.5	2.4	47	4.6	53	0.979
August 2	Nd	16.30–19.06	~0.5	SK04	2.5	2.3	50	4.6	50	0.976
		13.07–14.03	~0.3	SK18	2.0	2.0	69	3.4	31	0.970
		14.15–15.25	~0.3	SK19	2.0	1.9	78	2.7	22	0.966
August 3	17.47	18.00–18.12	~0.8	SK21	1.5	1.0	94	4.1	6	0.940

Eruption times (according to communications from the Sakurajima Volcano Observatory (SVO)) are reported together with the time of collection and the map location codes (see map in Figure 1). Eruption times not reported on SVO archives are indicated as “Nd” and refer probably to low intensity events. SP1 and SP2 represent the coarse and fine subpopulations (see the text for more details). The Determination coefficient R² indicates the goodness of fit associated with the deconvolution of the grainsize in two Gaussian subpopulations (i.e., SP1 and SP2).

aggregated ash around a central core formed by one or more particles (up to 4) with size 1–2 orders of magnitude larger than coating ash. PC3 is the most frequently observed particle cluster category (55–65% of all aggregates observed in videos; Figure 5).

Grain Size Distribution of the Aggregate Shells

The GSD of the aggregate shells (Figure 4) was determined, through SEM analysis, for 10 out of the 62 aggregates captured by HS-HR video footages (Supplementary Table S3); these aggregates were collected during 2 days of activity (August 2–3). For all the aggregates, the main measured (or calculated) physical parameters and the statistical parameters describing the GSDs are reported in Table 3. Also, in this case, GSDs were deconvoluted into two main Gaussian subpopulations (SPs), with the ratio between the relative weight of the two SPs (“SP-ratio” in Table 3) being one of the distinctive features between the different types of GSD.

Two main types of GSDs are distinguished for the aggregate shells (Figure 4), mostly based on the mode, the values of graphical skewness (Folk, 1966), and the proportion between the internal subpopulations (i.e., SP-ratio = relative weight of SP2/relative weight of SP1):

- Type 1: bimodal GSDs with the main mode comprised between 4 and 6 ϕ , and a secondary mode (where present) peaked at around 7 ϕ (Figures 4A,B). This GSD type is characterized by nearly symmetrical to positively skewed distributions (Folk, 1966) and a value of skewness mostly comprised between 0.09 and 0.49, with a single value up to 0.80 (Table 3). Both the SP1 and the SP2 display similar volume fractions, with an SP-ratio ranging from 0.66 to 1.92 (Table 3).
- Type 2: bimodal GSDs with a more pronounced main mode peaked mostly around 4.5–5 ϕ ; a secondary mode peaked around 7–8 ϕ is also present in two samples (Figures 4C,D). This GSD type is strongly positively skewed, with skewness values ranging from 0.53 to 0.75; only one sample shows a lower value at 0.02 (Table 3). The coarser SP represents a large volume fraction of the whole GSD (SP-ratio between 0.30 and 0.57; Table 3).

The two types of GSDs can be roughly related to the aggregate characteristics derived by both the HS-HR videos and the analysis of adhesive paper (Table 3):

- Shells with Type 1 GSD are mainly associated with aggregates with a thick, fine-ash rind completely enveloping a core formed by one or more larger clasts (classified as PC3) (e.g., samples 16sk19 and 21sk21; Figures 4A,B).
- Shells with Type 2 GSD are mostly related to aggregates with very thin coatings that do not form a discrete and thick rind (classified as PC2) (e.g., samples 20SK20 or 10SK21; Figures 4C,D).

TABLE 3 | Synoptic table reporting data of the aggregates collected during August 2–3.

Aggregate ID	Collection time (JST)	Available data	Aggregate			Core		Aggregate shell			
			Size (μm)	Terminal velocity (m/s)	Density (kg/m ³)	Size (μm)	Density (kg/m ³)	GSD type	SP-ratio	Median (φ)	Skew
16SK19	August 2, 14:54:30	Video/GSD/Core	362 ± 35	0.89 ± 0.08	561 [475, 751]	202	2,648	Type 1	1.55	4.6 (41 μm)	0.32
17SK19	August 2, 14:56:15	Video/Core	441 ± 31	1.52 ± 0.05	854 [761, 1,000]	288	2,618	—	—	—	—
18SK19	August 2, 15:04:54	Video/Core	268 ± 20	1.56 ± 0.07	1,783 [1,574, 2,094]	260	2,606	—	—	—	—
19SK19	August 2, 15:08:15	Video/GSD/Core	290 ± 30	1.14 ± 0.1	1,121 [964, 1,576]	205	2,647	Type 2	0.30	4.8 (33 μm)	0.62
20SK20	August 2, 16:47:00	Video/GSD/Core	559 ± 38	2.14 ± 0.01	804 [739, 911]	474	2,551	Type 2	0.37	5.9 (17 μm)	0.53
21SK20	August 2, 16:49:23	Video/GSD/Core	237 ± 18	1.38 ± 0.01	1,778 [1,590, 2,066]	232	2,628	Type 1	1.92	6.3 (13 μm)	0.30
22SK20	August 2, 16:53:55	Video/GSD/Core	495 ± 39	2.7 ± 0.05	1,432 [1,303, 1,704]	487	2,510	Type 2	0.26	5.9 (17 μm)	0.76
23SK20	August 2, 17:02:41	Video/GSD/Core	269 ± 25	1.52 ± 0.08	1,951 [1,697, 2,546]	262	2,621	—	—	—	—
1SK21	August 3, 18:04:06	Video/Core	787 ± 54	2.92 ± 0.01	831 [766, 943]	755	2,451	—	—	—	—
2SK21	August 3, 18:04:07	Video/GSD/Core	757 ± 55	2.83 ± 0.01	848 [779, 974]	677	2,479	Type 1	0.66	3.8 (72 μm)	0.80
4SK21	August 3, 18:04:09	Core	775 ± 54	2.71 ± 0.03	739 [674, 838]	584	2,512	—	—	—	—
7SK21	August 3, 18:04:10	Core	830 ± 61	2.8 ± 0.09	722 [663, 848]	581	2,513	—	—	—	—
10SK21	August 3, 18:04:12	GSD	—	—	—	—	—	Type 2	0.58	7.5 (6 μm)	0.03
15SK21	August 3, 18:08:47	GSD	—	—	—	—	—	Type 2	0.35	5.4 (24 μm)	0.65
16SK21	August 3, 18:08:48	Video/Core	621 ± 47	1.87 ± 0.06	617 [560, 736]	427	2,568	—	—	—	—
19SK21	August 3, 18:08:51	Video/GSD/Core	504 ± 36	1.61 ± 0.02	677 [615, 779]	413	2,573	Type 1	0.76	5.1 (29 μm)	0.09
21SK21	August 3, 18:08:52	Video/GSD/Core	613 ± 42	1.38 ± 0.01	382 [349, 434]	388	2,582	Type 1	0.76	5.2 (27 μm)	0.49
27SK21	August 3, 18:08:55	Video/Core	675 ± 50	1.29 ± 0.01	307 [281, 356]	373	2,587	—	—	—	—
28SK21	August 3, 18:08:56	Core	—	—	—	260	2,628	—	—	—	—

GSD, grain size distribution; HS-HR, high-speed, high-resolution. The third column clarifies the source and type of available information (Video: HS video; GSD: grain size of associated deposit collected in tray; Core: information on aggregates core). Statistic of the grain size distribution of the aggregate shells (when available) are reported (SP-ratio, Median, Skewness) together with physical and aerodynamical parameters measured thanks to the analysis of the HS-HR videos (size and density of both aggregate and core and velocity of aggregate). Among the aerodynamical parameters, the values of density for each aggregate are also reported (first value outside brackets), calculated as the mode of the generated distribution for density using the Monte Carlo simulations. Density values are listed together with their associated uncertainties, equal to the 68% confidence interval of the generated distribution and displayed as the value corresponding to the 16th and 84th percentile [ρ_{pc16}^{pc16} ; ρ_{pc84}^{pc84}] of the distribution. Aerodynamical parameters relative to samples 4SK21 and 21SK21 are taken from Bagheri and Bonadonna (2016). SP-ratio is the ratio between the two subpopulations (see main text for details).

The dimension of the cores increases with the aggregate size (Figure 4E), although no clear relation appears between the aggregate size and the GSD of the shell (Table 3). In addition, the diameter of the core in PC2 and PC3 aggregates ranges between 0.5 and 2.5φ (between 180 and 710 μm) resulting in several (up to 2) orders of magnitude larger than the particles forming the shell (Figure 4F). It is also interesting to note that the GSD of the tephra samples corresponding to the aggregates collected on August 2–3 are bimodal (orange and dark blue lines in Figure 3). Importantly, the average GSD of the shell of all the aggregates (green curve in Figure 4F) and the size of aggregate cores (red circles in Figure 4F) well correlate with the subpopulations SP2 and SP1 (Table 2) of the of tephra samples, respectively (blue curve in Figure 4F). Since the shell of PC3 is thicker than the shell of PC2 aggregates, we suggest that SP2 of tephra sample GSD mostly contribute to the formation of the external shell of PC3 aggregates.

Aerodynamics of Aggregates from High-Speed, High-Resolution Videos

Obtained dataset on particle settling dynamics and textural features resulted in a larger database compared with previous studies (e.g., Taddeucci et al., 2011; Bagheri et al., 2016; Miwa et al., 2020). Results of HS-HR video analysis (in terms of the aggregate terminal velocity, density and size) are shown in Figure 5 (and summarized in Supplementary Table S3). A clustering of the aggregate aerodynamics with the day of collection (different colors

in Figure 5) is observed. In addition, indicative trends relating the physical properties of the three different types of aggregates that were observed (i.e., PC1, PC2, and PC3) can be tentatively traced based on visual identification (gray dashed lines; Figure 5). In particular, PC1, PC2, and PC3 were distinguished based on a qualitative assessment of the amount of material left on the adhesive paper at the moment of impact.

Measured aggregate sizes range between 200 and 1,200 μm (Supplementary Table S3). Corresponding terminal velocity varies between 0.5 and 4 m/s, with a large variability (up to 100%) observed for aggregates of similar size. The derived density values range between 250 and 2,000 kg/m³. In many cases, PC3 were clearly recognized at impact on the adhesive paper, where the external shell disaggregated and deposited while coarse-grained particles forming the core bounced away. Size of measured cores varies between 200 and 750 μm. Furthermore, in few cases large particles having diameters comprised in the range of 90–250 μm were observed to bounce away together with cores at impact with the adhesive papers. Terminal velocity of the aggregate cores (diamonds and triangles in Figures 5A,B) was calculated using Eq. 2, with volume estimates based on the three measured diameters from videos (Feret diameters: *L*, *I*, and *S*) and the density of the cores estimated according to the density-size trend found by Bagheri et al. (2016). Density values, ranging between 2,450 and 2,700 kg/m³, are in agreement with the typical density of Sakurajima magmas (Miwa et al., 2009; Hickey et al., 2016), and with values derived for similar particles by Bagheri

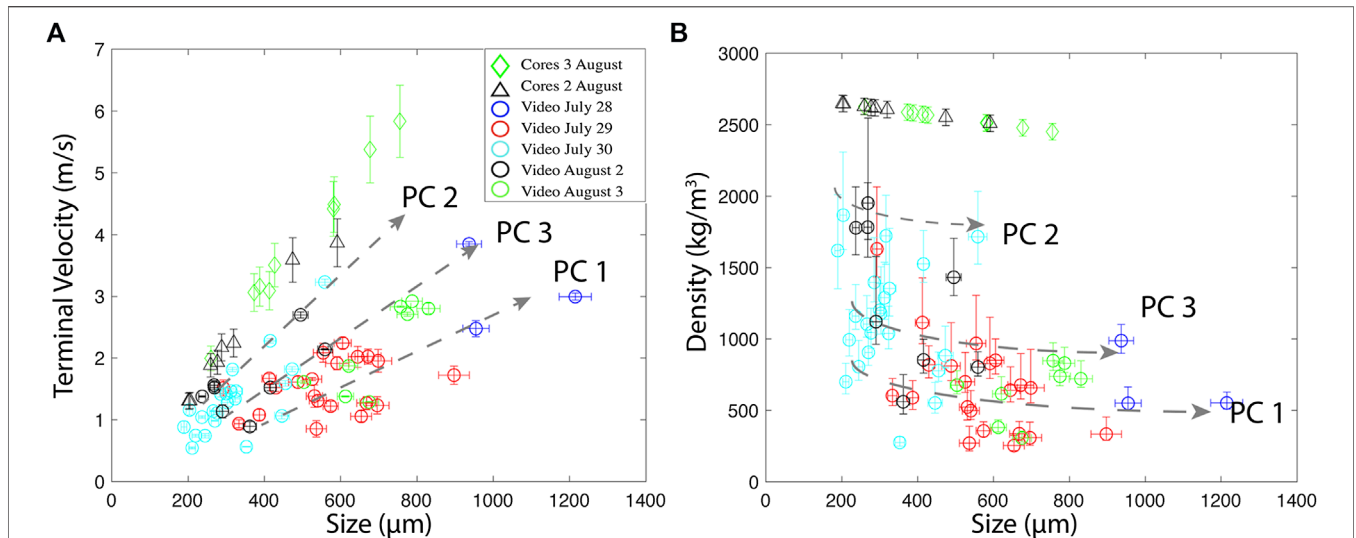


FIGURE 5 | Aerodynamic properties of aggregates (circles) and aggregate cores (triangles and diamonds) analyzed with HS-HR camera (colors refer to the day of collection). Terminal velocity of aggregates is measured directly from videos; terminal velocity of cores is calculated with Eq. 2 based on the density derived from the density-size trend obtained by Bagheri et al. (2016). **(A)** Terminal velocity against size, and **(B)** aggregate density against size. Dotted arrows define different aggregate types in the space velocity-density-size determined based on visual observations (see main text for more details).

et al. (2016). Terminal velocity, for these particles, ranges between 1 and 6 m/s and is strongly controlled by size. We assume that the trends defined by the cores (diamond and triangle markers in Figures 5A,B), of velocity and density vs. size, can be considered as representative of the aerodynamic behavior of individually falling particles (i.e., not aggregated particles). Consequently, these trends were taken as a reference to better interpret the aerodynamic behavior of the measured aggregates. Aggregates observed in the analyzed HS-HR footages (Figure 5A) generally show a slower increase of terminal velocity with size compared to those calculated for cores, although with a larger scatter.

Iso-velocity sections in the space density—aggregate diameter—terminal velocity clearly show how a given range of terminal velocity can be associated with aggregates of very different size and bulk density (Figure 6). The type of the aggregates collected on August 2–3, visually determined during the video analysis, is specified with labels in the diagram, in order to ease the interpretation of the presented aerodynamics data.

The smallest aggregates (<400 µm) are associated with the lowest terminal velocity (<2 m/s), the highest density values and the largest density range (mostly 1,000–2,000 kg/m³; Figures 6A,B). Three PC2 and one PC3 with low density (around 500 kg/m³) fall in this space (Figure 6B). On the other hand, large aggregates (>400 µm) generally correspond to lower density values (<800 kg/m³) and have terminal velocities between 1 and 3 m/s (Figures 6B–D). The majority of the identified aggregates from August 2–3 falling in this space are PC3. In general, less than 15% of aggregates fall with velocity lower than 1 m/s, and 60% fall with velocity in between 1 and 2 m/s. Velocities higher than 2 m/s are quite uncommon and are generally associated with the cores (diamonds and triangles in Figure 6D).

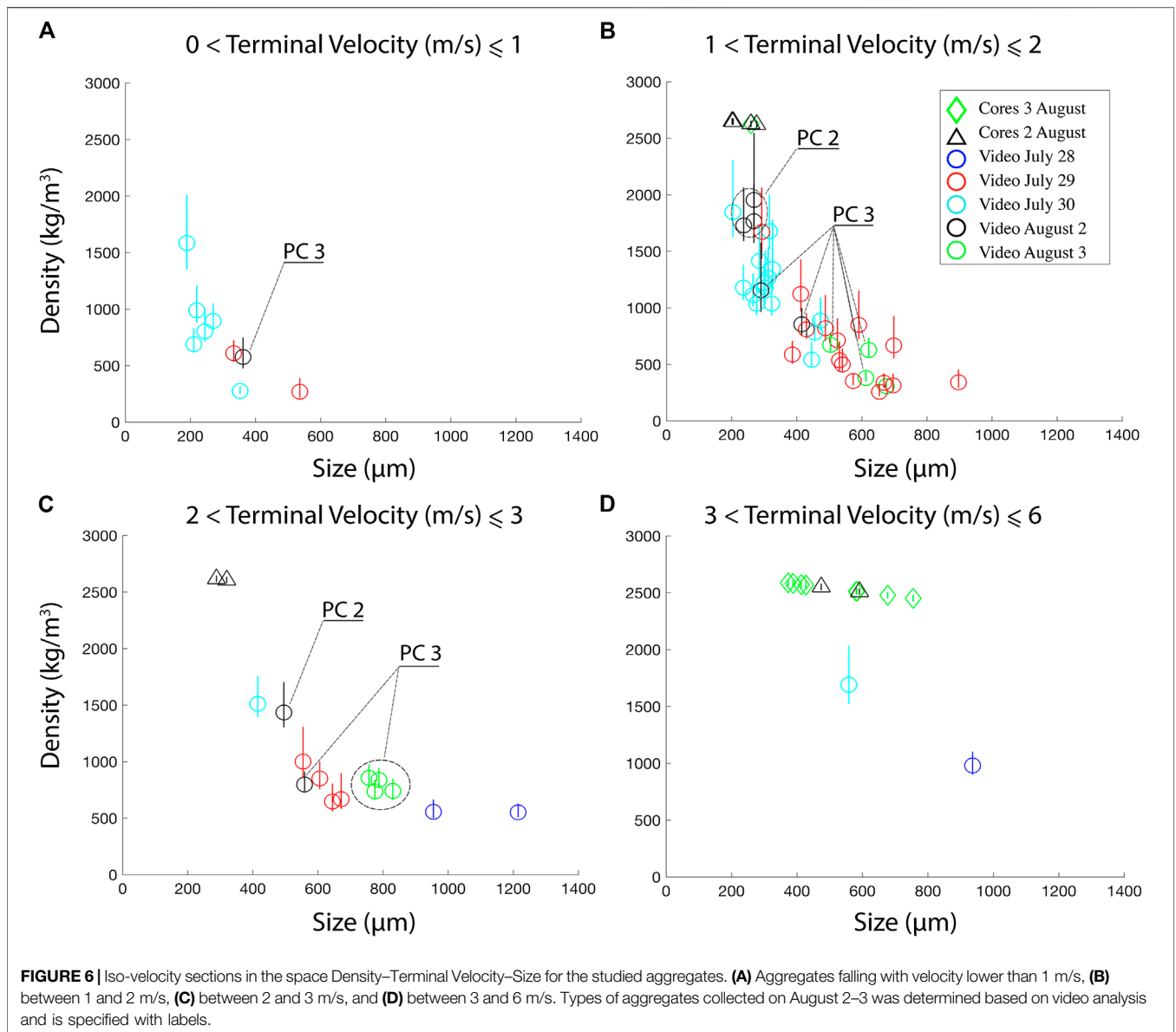
Information relative to the internal structure of selected aggregates collected on August 2–3 are presented in Figure 7.

Here, the thickness and the relative volume fraction of the shell with respect to the whole aggregate are compared with the derived density of 11 PC3 and 4 PC2 that were visually identified from HS-HR videos. Based on the evidences reported in Figures 5, 6, generally, PC2 aggregates are characterized by a higher density and a lower volume fraction of the shell with respect to PC3 aggregates, while the thickness of the shell is largely variable in both aggregate types. In particular, the measured PC2 aggregates are characterized by density values variable in the range of 1,500 and 2,000 kg/m³, and a thickness of the shell between 10 and 80 µm (Figure 7A). On the other hand, the PC3 reported here have density values in the range 400–1,200 kg/m³ and a shell thickness between 35 and 200 µm (Figure 7A). A preliminary distinction of the variability of the typical structural characteristics of PC2 and PC3 aggregates was tempted in Figure 7B. In particular, these data indicate a volume fraction of the shell mostly >40% for the PC3 aggregates, associated with an aggregate density generally lower than 1,200 kg/m³. On the other hand, PC2 aggregates are characterized by density values higher than 1,200 kg/m³, and a relative volume fraction of the shell typically <60%. A sort of overlap area, in which aggregates can have intermediate shell-volume fraction between that typical of PC2 and PC3, was revealed for volume fractions of the shell in the range 40–60%.

DISCUSSION

Grain Size Distribution of Tephra Samples and of Aggregating Particles

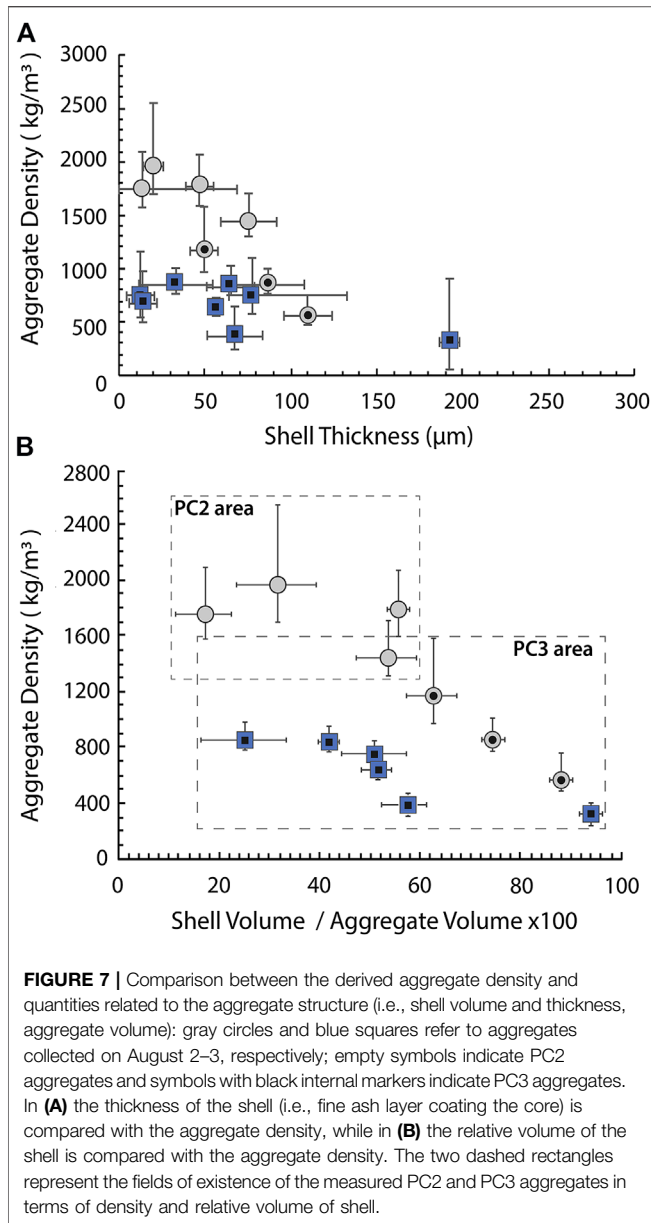
The GSDs of tephra samples are mostly bimodal and can be described as the result of the superposition of two Gaussian subpopulations (SP1 and SP2) (Figure 3; Table 2). The internal



structure of aggregates, characterized by the presence of a core and a shell of fine aggregating ash, well correlates with the bimodal GSD of tephra samples. In particular, the average GSD of the aggregate shells corresponds to the fine subpopulation (SP2) of the tephra GSDs, while the mode of their coarse subpopulation (SP1) corresponds to the size of the internal cores of aggregates (Figure 4F; Table 3). Furthermore, direct observations indicate that ash aggregation was always active during sedimentation. The variable presence of SP2 in all the ash deposits can be thus considered a direct result of ash aggregation efficiency during the different eruptions. The increasing amount of SP2 generally observed in samples at increasing cross-wind distance (Table 2) could be also related to an increasing off-axis occurrence of low-density aggregates, generally characterized by a thicker, poorly compacted, low-density external shell formed by fine-grained particles. The

relative amount of SP2 in the bulk samples is always lower than SP1, since the fine ash forming the shell of the aggregates only represents, on a weight basis, a low proportion (from few percent to a maximum of around 50 wt%) of the total GSD of the most common aggregates (PC2 and PC3, dominated by the core particle). The GSD of aggregate shells compares well with those reported in Bonadonna et al. (2011), who estimated an $Md\phi$ of 5.4 for the aggregates of the 2010 Eyjafjallajökull eruption, and in Bagheri et al. (2016), who measured $Md\phi$ between 4.5 and 5.5 ϕ for other PC3 Sakurajima aggregates. These observations confirm that the process of aggregation is highly efficient for ash finer than around 4–5 ϕ (i.e., around 45 μ m) (Figure 4F; Table 3).

The analysis of the video footages also reveals that aggregates are rarely larger than 800–900 μ m (Supplementary Table S3), and cores found in the aggregates rarely exceed 500 μ m, confirming thus the results reported in Bagheri et al. (2016) that found a core



size comprised between 200 and 600 μm . We suggest that the cores of PC3 as well as the poorly covered particles of PC2 contributed to form SP1, while the SP2 present in each sample is mostly associated with the shell of the PC3 aggregates and, albeit in minor proportion, also with particles forming the shell of PC2 and those related to PC1. As the ash particles forming the shell of the aggregates represent a largely variable proportion of each aggregate in terms of volume (Figure 7B), we conclude that GSD of tephra samples is the complex result of the accumulation of different types of aggregated particles, each contributing in different proportions to SP1 and to the early fallout of the finer-grained fraction (SP2). On the other hand, the variability observed in the GSDs of aggregating ash (Figure 4; Table 3) is in accord with the difference revealed in internal structures of the identified aggregates (Figures 6, 7). The GSD of aggregating ash

is generally bimodal and shows a positively skewed distribution (Figures 4A–C). In particular, PC3 aggregates, showing a distinct external shell formed by fine ash, are indeed characterized by a bimodal, dispersed GSD (aggregates of Figures 4A,B), very different from that shown by the ash adhering to coated particles PC2, which is generally strongly peaked and fine to very fine-grained (aggregates of Figures 4C,D). This results in a general higher density of PC2 with respect to PC3 aggregates, since they are characterized by lower relative volume fractions of the shell respect to the aggregate (Figure 7).

In the context of the same eruption, these two types of aggregates possibly indicate either variable conditions of ash aggregation under different eruptive and environmental conditions (in terms, for example, of ash concentration), or different time steps of the same aggregation process around a core. Unfortunately, PC1 aggregates were only observed in videos (Figure 5) but were not collected in adhesive paper and, therefore, the associated structure and GSD could not be analyzed and compared with the characteristic of PC2 and PC3 types.

Dynamics of Aggregate Deposition

The analysis of the HS-HR footages allowed us to characterize the aerodynamic behavior of falling aggregates and to describe their internal structure before impact and disruption on the adhesive paper. The analysis of the filmed aggregates revealed a wide range in both terminal velocity and density (Figure 5). Measured terminal velocities are between 0.5 and 4 m/s, with most values between 1 and 2 m/s (Figure 6). Density and size vary in a wide range (250–2,000 kg/m^3 and 200–1,200 μm , respectively). In particular, Figure 6 shows a large variation either in the values of density and terminal velocity for aggregates having a size in the range of 200–650 μm . This aspect suggests that, given an average density of single particles (non-aggregated) in the range of 2,400–2,700 kg/m^3 , the small aggregates (200–300 μm) associated with the highest density (>1,000 kg/m^3) and velocity in the range of 1 and 2 m/s, are possibly formed by large particles covered by a very thin and discontinuous shell of ash (PC2). If this is the case, the thickness of the shell has a minor effect on the aerodynamics of the whole aggregate, whose behavior is similar to non-aggregated particles. Conversely, large aggregates (>350 μm) falling with velocities between 1 and 3 m/s, are always associated with a density lower than 1,000 kg/m^3 , suggesting the presence of a thick ash shell, which represents a large fraction of the total volume of the aggregate (PC3). This strongly affects the aerodynamics of these aggregates, making them clearly distinct from single particles.

All these values are in good agreement with the results of Bagheri et al. (2016) and Miwa et al. (2020) for similar eruptions of Sakurajima volcano, even though Miwa et al. (2020) also report some higher values of terminal velocity (i.e., 6.5 m/s), corresponding however to unlikely density for volcanic particles (i.e., 4,400 kg/m^3).

The very similar meteorological conditions during sample collection in the eruptions of August 2–3 (Figure 2) suggest a stronger dependence of the aggregation modalities on eruptive conditions and aggregation dynamics rather than on atmospheric parameters. In particular, the few aggregates measured on July 28

show size greater than 900 μm and density lower than 1,000 kg/m^3 , while aggregates collected on July 30 are all below 500 μm in size and have a largely variable density, between 500 and 2,000 kg/m^3 (**Figure 5**). Aggregates from July 29 and August 3 have instead a large size (between 400 and 800 μm) associated with density values lower than 1,000 kg/m^3 . Moreover, the relation between the relative volume of the shell with the density of the aggregates collected on August 2–3 confirmed an important difference between physical and structural characteristics of PC2 and PC3 aggregates (**Figure 7**). The same data also indicate that aggregates collected on August 2 slightly differ from those collected on August 3 since the PC3 aggregates collected during this latter eruption are less dense and characterized by a lower relative volume of the shell (**Figure 7B**). These high-detail data provided for selected aggregates are well in accord with the trends shown by the general dataset (**Figure 5**) where, again, there is a clear relationship between the aerodynamics of aggregates (and hence structure) and day of collection. Finally, the link between the internal structure, and hence the type of aggregates, and their aerodynamic behavior is unraveled in **Figure 6**, where the type of selected aggregates collected on August 2–3 is indicated. These aggregates, together with their cores (i.e., single particles), represent a reference useful to interpret the nature of all the other aggregates measured in the context of this study, and justify the trends traced in **Figure 5**. The critical analysis of all the presented data, combined with direct observations of the video footages, can inform about the nature of the different falling aggregates allowing the quantitative characterisation of three different aggregate categories, reported below in decreasing order of abundance:

- (1) PC3: aggregates with diameters comprised between 200 and 900 μm , velocity in the range 0.5–3.5 m/s and density between 500 and 1,500 kg/m^3 . They represent the majority of the aggregates falling during the entire period of observation (with around 40 aggregates detected) and are characterized by an internal core and an external shell which is largely variable in thickness. The relative volume of the shell with respect to the aggregate is typically higher than 55%. The thickness of the shell controls the density, with the lowest calculated values (around 500 kg/m^3) corresponding to aggregates having a shell thickness around 200 μm that represents the 90% of the volume of the whole aggregate (**Figure 7A**). The structural framework of these aggregates shows also a good relation with the day of collection, being particles collected on August 2 generally characterized by a higher volume fraction of the external shell (**Figure 7B**). This group of aggregates corresponds to the cored clusters observed by Bagheri et al. (2016) and, possibly, by Miwa et al. (2020).
- (2) PC2: some aggregates from July 30 and August 2, plotting close to the core trend-line and showing high velocities compared with the diameters (up to 3 m/s and 200–550 μm , respectively; **Figure 5A**), possibly represent the PC2 of Brown et al. (2012), with an associated density of 1,500–2,000 kg/m^3 (**Figure 5B**). The aerodynamic properties of these aggregates, similar to those of single particles, can be explained as related to the presence of a

very thin, discontinuous layer of coating ash on a coarse particle, which only weakly influenced its fallout behavior. Normally, the relative volume of the shell is below 30%.

- (3) PC1: few aggregates (<10) showing large diameters and very low density (350–1,200 μm and <500 kg/m^3 , respectively; **Figure 5B**), together with a terminal velocity generally below 2 m/s (except for two of the coarser aggregates, larger than 900 μm ; **Figure 5B**). These aggregates, not always clearly distinguishable on samples collected on adhesive papers, can be associated to PC1 of Brown et al. (2012). The low density is similar to that estimated for electrostatically aggregated ash by James et al. (2003).

Particle clusters similar to those analyzed and described here are frequently observed during fallout from ash-dominated eruptions worldwide. As a consequence, the presented dataset of measurements is of primary importance particularly for the in-depth characterization of natural ash aggregates. In particular, data collected on the numerous PC3 aggregates observed here represent a novel, very important step forward in the recognition of the effects of aggregation on ash sedimentation and formation of tephra deposits. Even though these aggregates are typically not preserved in the deposits, they have been shown to control the main features of the resulting ash deposit due to their abundance. In fact, their bimodal GSD related to a thick, fine-grained external shell mantling few (although mass-dominant) coarser particles, well correlates with the GSD bimodality of the associated ash deposits.

CONCLUSIONS

The presented results form a wide and reliable dataset of particle clusters including important physical and aerodynamic parameters (i.e., terminal velocity, density and size), which are extremely valuable for the physical characterisation of aggregates and aggregating ash, and for the validation of volcanic ash transport and dispersal models. Three main types of aggregates [Cored Clusters (PC3), Coated Particles (PC2), and Ash Clusters (PC1)] were identified and characterized based on direct measurements of size and terminal velocity, on the derived estimates of their density and on their internal characteristics: size of the core, GSD of the external shell, and relative volume fraction of the aggregating shell. The discovery of highly variable limits for density and terminal velocity of aggregates collected at the same time and location, along with the accurate quantification of the average grain size and the relative volume fraction of the aggregating ash internal to PC2 and PC3 aggregates and the typical size of the inner cores, shed new light on the characterisation volcanic ash aggregates. Our detailed investigations show how:

- PC3-type is the most abundant group representing more than 60% of the observed aggregates; they show important variations in size (200–900 μm) and in density (500–1,500 kg/m^3). PC3 size is positively correlated with the size of the internal core, while aggregate density shows a negative relation with the thickness of the shell, with the thickest shells (90% in volume respect to the aggregate)

being associated with an overall low density of the aggregate (down to around 500 kg/m^3) (Figure 7).

- The relative volume fraction of the external shell of PC3 with respect to the whole aggregate is mostly $>40\%$. The GSDs of the ash enclosed in the shell of these aggregates display a positively skewed and bimodal GSD, with around 50% of the associated tephra-fallout sample represented by SP2 and the modes peaked around $5-6\phi$ (Figure 4). Considering that PC3 are abundant during all the investigated period, and the shell of PC3 can represent a significant volume fraction of the whole aggregate volume ($>40\%$ vol.), we suggest this category as the one that mostly controlled the dynamics of the fine ash dispersal during the analyzed eruptions at Sakurajima. PC2 aggregates have the highest density, in the range of $1,500-2,000 \text{ kg/m}^3$, and are characterized by terminal velocities similar to those calculated for single particles, since they have a very thin external shell.
- The relative volume of the shell of PC2 aggregates is comprised between 10 and 60% vol. (Figure 7). The shell GSD is highly sorted and peaked around $6-8\phi$, with low deposit fractions (around 25%) represented by the SP2 (Figure 4). We suggest that this median size is mainly related to the availability of fine ash within the eruptive plume.
- Aggregate shells consist of ash particles $<45 \mu\text{m}$ for both PC2 and PC3 (Figure 4). Moreover, the GSD of tephra samples is strongly influenced by the type and the availability of aggregates in the deposits, being the cores and the shells of particle clusters similar in size to the coarser and finer subpopulation of tephra samples, respectively (Figure 4). Despite the identification of a semi-quantitative limit to distinguish between PC2 and PC3 based on the aggregate density (approx. $1,200 \text{ kg/m}^3$) and the relative volume of the shell (approx. $40-60\%$ vol.), we suggest that a progressive transition should exist between the structural features of these two categories of aggregates. The few detected PC1, showing large diameters ($400-1,000 \mu\text{m}$) and very low density ($200-500 \text{ kg/m}^3$), are the result of fine ash aggregation in the absence of an aggregating core. Due to their low abundances, no PC1 aggregate was directly collected with adhesive tapes, and consequently no GSD was provided for this type of aggregates.
- The physical parameters (i.e., size, density, and terminal velocity) of aggregates show a very wide variation among the different eruptive events, with the largest and least dense aggregates being associated with the activity of July 28, and the smallest and highest density aggregates associated with the activity of July 30 (eruption registered at 17.03 JST) (Figures 5, 6). A strong relation was found between the aggregate aerodynamics and structure (and hence type), with the day of activity. In particular, we note that size and density of aggregates analyzed during August 2-3 are variable, with the largest and least dense PC3 aggregates being associated with the activity of August 3. According to the stable atmospheric conditions at the time of aggregate formation and collection, differences in the internal structure observed between the aggregates of the different days of activity could be mostly related to primary

differences in eruptive conditions (e.g., ash concentration and grain size of the eruptive mixture in the plume).

- The combination of kinetic data, measured from HS-HR imaging, with information extracted from tephra samples and aggregates collected on adhesive papers, confirmed to be a state-of-the-art technique necessary to provide important insights into the understanding of aggregation processes, and the associated impact on fallout dynamics. The statistical treatment of aerodynamic and physical data, and the large number of investigated aggregates make the presented results a benchmark reference for the validation and calibration of numerical schemes for particle aggregation. Such a wide dataset derived from our multidisciplinary strategy is particularly important for the characterisation of particle clusters, which have recently been shown to be among the most common aggregate types during ash-rich fallout but are not preserved in tephra deposits. In particular the abundance of PC3 aggregates reconciles the presence of a large amount of fine ash (aggregate shell) with coarse ash (aggregate core) and better explains GSD bimodality of tephra deposits, high aggregate settling velocities with respect to PC1 and low aggregate settling velocities with respect to PC2.

AUTHOR'S NOTE

The work is part of the PhD thesis of PG.

DATA AVAILABILITY STATEMENT

The original contributions presented in the study are included in the article/**Supplementary Materials**, further inquiries can be directed to the corresponding author/s.

AUTHOR CONTRIBUTIONS

PG conducted this work as part of his PhD at the University of Florence. He analyzed and processed the data collected at Sakurajima volcano (Japan) by ER, GB and CB. ER, CB, MP, and RC largely contributed to the interpretation of the results. All authors were involved in the writing and finalization of the manuscript.

FUNDING

This work was supported by the Swiss National Science Foundation (Grant No. 200021_156255), and work of PG and RC was supported by funds of the University of Florence to RC.

SUPPLEMENTARY MATERIAL

The Supplementary Material for this article can be found online at: <https://www.frontiersin.org/articles/10.3389/feart.2020.575874/full#supplementary-material>

REFERENCES

- Bagheri, G., and Bonadonna, C. (2016). On the drag of freely falling non-spherical particles. *Powder Technol.* 301, 526–544. doi:10.1016/j.powtec.2016.06.015
- Bagheri, G., Rossi, E., Biass, S., and Bonadonna, C. (2016). Timing and nature of volcanic particle clusters based on field and numerical investigations. *J. Volcanol. Geotherm. Res.* 327, 520–530. doi:10.1016/j.jvolgeores.2016.09.009
- Bonadonna, C., Folch, A., Loughlin, S., and Puempel, H. (2012). Future developments in modelling and monitoring of volcanic ash clouds: outcomes from the first IAVCEI-WMO workshop on ash dispersal forecast and civil aviation. *Bull. Volcanol.* 74 (1), 1–10. doi:10.1007/s00445-011-0508-6
- Bonadonna, C., Genco, R., Gouhier, M., Pistolesi, M., Cioni, R., Alfano, F., et al. (2011). Tephra sedimentation during the 2010 Eyjafjallajökull eruption (Iceland) from deposit, radar, and satellite observations. *J. Geophys. Res. Solid Earth* 116 (12). doi:10.1029/2011jb008462
- Bonadonna, C., Macedonio, G., and Sparks, R. S. J. (2002a). Numerical modelling of tephra fallout associated with dome collapses and Vulcanian explosions: application to hazard assessment on Montserrat. *Geol. Soc. Lond. Mem.* 21 (1), 517–537. doi:10.1144/gsl.mem.2002.021.01.23
- Bonadonna, C., Mayberry, G. C., Calder, E. S., Sparks, R. S. J., Choux, C., Calder, E. S., et al. (2002b). Tephra fallout in the eruption of Soufrière Hills Volcano, Montserrat. *Geol. Soc. Lond. Mem.* 21 (1), 483–516. doi:10.1144/gsl.mem.2002.021.01.22
- Brown, R. J., Bonadonna, C., and Durant, A. J. (2012). A review of volcanic ash aggregation. *Phys. Chem. Earth* 45–46, 65–78. doi:10.1016/j.pce.2011.11.001
- Burns, F. A., Bonadonna, C., Pioli, L., Cole, P. D., and Stinton, A. (2017). Ash aggregation during the February 11, 2010 partial dome collapse of the Soufrière Hills Volcano, Montserrat. *J. Volcanol. Geotherm. Res.* 335, 92–112. doi:10.1016/j.jvolgeores.2017.01.024
- Cornell, W., Carey, S., and Sigurdsson, H. (1983). Computer simulation of transport and deposition of the Campanian Y-5 ash. *J. Volcanol. Geotherm. Res.* 17, 89–109. doi:10.1016/0377-0273(83)90063-x
- Costa, A., Folch, A., and Macedonio, G. (2010). A model for wet aggregation of ash particles in volcanic plumes and clouds: I. Theoretical formulation. *J. Geophys. Res. Solid Earth* 115, B9. doi:10.1029/2009jb007175
- Durant, A. J. (2015). Research focus: toward a realistic formulation of fine-ash lifetime in volcanic clouds. *Geology* 43, 271–272. doi:10.1130/focus032015.1
- Durant, A. J., Rose, W. I., Sarna-Wojcicki, A. M., Carey, S., and Volentik, A. C. M. (2009). Hydrometeor-enhanced tephra sedimentation: constraints from the May 18, 1980 eruption of Mount St. Helens. *J. Geophys. Res. Solid Earth* 114, B3. doi:10.1029/2008jb005756
- Folk, R. L. (1966). A review of grain-size parameters. *Sedimentology* 6.2 (1966), 73–93.
- Gilbert, J. S., and Lane, S. J. (1994). The origin of accretionary lapilli. *Bull. Volcanol.* 56 (5), 398–411.
- Guffanti, M., Casadevall, T. J., and Budding, K. (2010). *Encounters of aircraft with volcanic ash clouds: a compilation of known incidents, 1953–2009*. US Department of Interior, US Geological Survey.
- Hickey, J., Gottsmann, J., Nakamichi, H., and Iguchi, M. (2016). Thermomechanical controls on magma supply and volcanic deformation: application to Aira caldera, Japan. *Sci. Rep.* 6, 1–10. doi:10.1038/srep32691
- Iguchi, M., Yakiwara, H., Tameguri, T., Hendrasto, M., and Hirabayashi, J.-i. (2008). Mechanism of explosive eruption revealed by geophysical observations at the Sakurajima, Suwanosejima and Semeru volcanoes. *J. Volcanol. Geotherm. Res.* 178 (1), 1–9. doi:10.1016/j.jvolgeores.2007.10.010
- Ishihara, K. (1985). Dynamical analysis of volcanic explosion. *J. Geodyn.* 3 (3), 327–349. doi:10.1016/0264-3707(85)90041-9
- James, M. R., Gilbert, J. S., and Lane, S. J. (2002). Experimental investigation of volcanic particle aggregation in the absence of a liquid phase. *J. Geophys. Res. Solid Earth* 107 (B9), ECV 4-1–ECV 4-13. doi:10.1029/2001jb000950
- James, M. R., Lane, J. S., and Gilbert, J. S. (2003). Density, construction, and drag coefficient of electrostatic volcanic ash aggregates. *J. Geophys. Res. Solid Earth* 108 (B9), 1–12. doi:10.1029/2002jb002011
- Jenkins, S. F., Wilson, T. M., Magill, C., Miller, V., Stewart, C., Blong, R., et al. (2015). “Volcanic ash fall hazard and risk,” in *Global volcanic hazards and risk*. Editors S. C., et al. (Cambridge: Cambridge University Press), 173–222.
- Miwa, T., Geshi, N., and Shinohara, H. (2013a). Temporal variation in volcanic ash texture during a Vulcanian eruption at the Sakurajima volcano, Japan. *J. Volcanol. Geotherm. Res.* 260, 80–89. doi:10.1016/j.jvolgeores.2013.05.010
- Miwa, T., Iriyama, Y., Nagai, M., and Nanayama, F. (2020). Sedimentation process of ashfall during a Vulcanian eruption as revealed by high-temporal-resolution grain size analysis and high-speed camera imaging. *Prog. Earth Planet. Sci.* 7 (1), 3. doi:10.1186/s40645-019-0316-8
- Miwa, T., Toramaru, A., and Iguchi, M. (2009). Correlations of volcanic ash texture with explosion earthquakes from Vulcanian eruptions at Sakurajima volcano, Japan. *J. Volcanol. Geotherm. Res.* 184 (3–4), 473–486. doi:10.1016/j.jvolgeores.2009.05.012
- Oba, N., Tomita, K., Yamamoto, M., Ohsako, N., and Inoue, K. (1980). Mineral and chemical composition, and mechanism of formation of volcanic ashes from Sakurajima volcano, Kyushu, Japan. *J. Japan. Assoc. Min. Petr. Econ. Geol.* 75 (10), 329–336. doi:10.2465/ganko1941.75.329
- Rose, W. I., and Durant, A. J. (2011). Fate of volcanic ash: aggregation and fallout. *Geology* 39 (9), 895–896. doi:10.1130/focus092011.1
- Schindelin, J., Arganda-Carreras, I., Frise, E., Kaynig, V., Longair, M., Pietzsch, T., et al. (2012). Fiji: an open-source platform for biological-image analysis. *Nat. Methods* 9, 676–682.
- Sorem, R. K. (1982). Volcanic ash clusters: tephra rafts and scavengers. *J. Volcanol. Geotherm. Res.* 13 (1), 63–71. doi:10.1016/0377-0273(82)90019-1
- Taddeucci, J., Scarlato, P., Montanaro, C., Cimarelli, C., Del Bello, E., Freda, C., et al. (2011). Aggregation-dominated ash settling from the Eyjafjallajökull volcanic cloud illuminated by field and laboratory high-speed imaging. *Geology* 39 (9), 891–894. doi:10.1130/G32016.1
- Textor, C., Graf, H. F., Herzog, M., Oberhuber, J. M., Rose, W. I., and Ernst, G. G. J. (2006). Volcanic particle aggregation in explosive eruption columns. Part II: numerical experiments. *J. Volcanol. Geotherm. Res.* 150 (4), 378–394. doi:10.1016/j.jvolgeores.2005.09.008
- Van Eaton, A. R., Muirhead, J. D., Wilson, C. J. N., and Cimarelli, C. (2012). Growth of volcanic ash aggregates in the presence of liquid water and ice: an experimental approach. *Bull. Volcanol.* 74, 1963–1984. doi:10.1007/s00445-012-0634-9
- Van Eaton, A. R., and Wilson, C. J. N. (2013). The nature, origins and distribution of ash aggregates in a large-scale wet eruption deposit: Oruanui, New Zealand. *J. Volcanol. Geotherm. Res.* 250, 129–154. doi:10.1016/j.jvolgeores.2012.10.016
- Veitch, G., and Woods, A. W. (2001). Particle aggregation in volcanic eruption columns. *J. Geophys. Res.* 106 (B11), 26425–26441. doi:10.1029/2000jb900343
- Vogel, A., Durant, A. J., Cassiani, M., Clarkson, R. J., Slaby, M., Diplas, S., et al. (2019). Simulation of volcanic ash ingestion into a large aero engine: particle–fan interactions. *J. Turbomach.* 141 (1). doi:10.1115/1.4041464
- Yamanoi, Y., Takeuchi, S., Okumura, S., Nakashima, S., and Yokoyama, T. (2008). Color measurements of volcanic ash deposits from three different styles of summit activity at Sakurajima volcano, Japan: conduit processes recorded in color of volcanic ash. *J. Volcanol. Geotherm. Res.* 178 (1), 81–93. doi:10.1016/j.jvolgeores.2007.11.013

Conflict of Interest: The authors declare that the research was conducted in the absence of any commercial or financial relationships that could be construed as a potential conflict of interest.

Copyright © 2020 Gabellini, Rossi, Bonadonna, Pistolesi, Bagheri and Cioni. This is an open-access article distributed under the terms of the Creative Commons Attribution License (CC BY). The use, distribution or reproduction in other forums is permitted, provided the original author(s) and the copyright owner(s) are credited and that the original publication in this journal is cited, in accordance with accepted academic practice. No use, distribution or reproduction is permitted which does not comply with these terms.